Available online at www.sciencedirect.com
SCIENCE DIRECT®
ELSEVIER
Journal of Magnetism and Magnetic Materials 300 (2006) 333–350
Journal of magnetism and magnetic materials
www.elsevier.com/locate/jmmm

Magnetostructural phase transitions of $DyFe_4Ge_2$: Part II Neutron diffraction

P. Schobinger-Papamantellos[a,*], J. Rodríguez-Carvajal[b], G. André, K.H.J. Buschow[c]

[a]*Laboratory of Crystallography, ETH-Hönggerberg HCI G512 CH-8093 Zürich, Switzerland*
[b]*Laboratoire Léon Brillouin, (CEA-CNRS) Saclay, 91191 Gif sur Yvette Cedex, France*
[c]*Van der Waals-Zeeman Institute, University of Amsterdam, NL-1018XE, Amsterdam*

Received 19 March 2005
Available online 16 June 2005

Abstract

We present the temperature magnetic phase diagram of the compound $DyFe_4Ge_2$ determined from neutron diffraction data for the entire magnetically ordered regime. $DyFe_4Ge_2$ undergoes at $T_N, T_c = 55\,K$ a simultaneous structural and magnetic transition of second order (or weakly first order) followed by two subsequent isostructural first-order magnetic transitions at $T_{ic2} = 45\,K$ and $T_{ic1} = 28K$:

$P4_2/mnm,\ T_N, T_c = 55\,K \rightarrow Cmmm, \mathbf{q}_1 = (0\,\frac{1}{2}0)$
$T_{ic2} = 45\,K \rightarrow \mathbf{q}_2 = (0\,q_y\,0) T_{ic1} = 28\,K \rightarrow \mathbf{q}_1.$

The re-entrant lock-in magnetic phase $\mathbf{q}_1 = (0\,\frac{1}{2}0)$ is stable in the high-temperature range T_{ic2}–T_N and in the low-temperature range 1.5 K–T_{ic1} while the incommensurately modulated $\mathbf{q}_2 = (0\,q_y\,0)$ magnetic phase is sandwiched in the intermediate range T_{ic1}–T_{ic2} between the two commensurate phases. The wave vector $\mathbf{q}_2$ has a temperature-dependent length with a minimum in the middle of the incommensurate range and corresponds to a multiaxial amplitude modulated phase. Symmetry analysis leads for both propagation vectors in *Cmmm* to a twofold and fourfold splitting of the tetragonal Dy 2*b* site and the Fe 8*i* sites, respectively. The low temperature $\mathbf{q}_1 = (0\,\frac{1}{2}0)$ and the $\mathbf{q}_2 = (0\,q_y\,0)$ phases correspond to 3D canted magnetic structures described by the irreducible representations (Irreps) $\Gamma_2 + \Gamma_3$ while the high-temperature $\mathbf{q}_1$ phase to 2D canted magnetic structures described by a single Irrep Γ_2. The T_{ic2} transition is connected with reorientations of both Fe and Dy moments.

PACS: 75.25.+z; 61.12.ld; 71.20.Eh; 75.80.+q

Keywords: Magnetic structure; Neutron diffraction; Rare earth alloys; Magnetoelastic transition

*Corresponding author. Tel: +41 44 632 3773; fax: +41 44 632 1133.
E-mail address: schobinger@mat.ethz.ch (P. Schobinger-Papamantellos).

0304-8853/$ - see front matter © 2005 Elsevier B.V. All rights reserved.
doi:10.1016/j.jmmm.2005.05.018

1. Introduction

The presently available results with regard to magnetic and structural properties of the RFe$_4$Ge$_2$ (R = Y, Er, Ho) compounds with magnetic and nonmagnetic rare earths are summarised as follows:

YFe$_4$Ge$_2$: For this compound, having a nonmagnetic rare earth, magnetic ordering occurs simultaneously with a first-order structural transition from tetragonal to orthorhombic symmetry [1]:

$$P4_2/mnm(T_N, T_c) = 43.5\,K \rightarrow Pnnm(\mathbf{q} = 0).$$

In *Pnnm* the Fe site splits into two sites. The symmetry breaking is connected with primary displacive order parameters involving shifts of the Fe atoms. This induces the symmetry-breaking tensile strains. The shifts of the Fe atoms with respect to the tetragonal phase have opposite signs along the a (dilatation) and b (contraction) axes. A planar canted antiferromagnetic arrangement, associated with the wave vector ($\mathbf{q} = 0$), with eight sublattices, is the ground state associated with a magnetic energy involving isotropic exchange and anisotropic interactions. The Fe ordered moment value at the lowest temperature of 1.5 K is the same for the two Fe orbits and equals 0.63(4) μ_B/Fe atom in good agreement with the Mössbauer data for the RFe$_4$Ge$_2$, R = Dy, Ho compounds [2,3].

In ErFe$_4$Ge$_2$ where the magnetostructural transition is associated with a double symmetry breaking occurring below $T_N, T_c = 44$ K [4,5]. The high temperature (*HT*) tetragonal phase disproportionates into two distinct phases of orthorhombic symmetry which coexist in form of domains in proportions varying with temperature. The transition paths are:

(a) $P4_2/mnm(T_N, T_c) = 44\,K \rightarrow Cmmm : (\mathbf{q} = (0\,\tfrac{1}{2}\,0))$

(b) $P4_2/mnm(T_N, T_c) = 44\,K \rightarrow Pnnm : (\mathbf{q} \neq 0)$ (minority phase).

The *Cmmm* phase is dominating the low temperature range (*LT*) 1.5–20 K and grows at the cost of the *Pnnm* phase on cooling. The latter phase reaches its maximal content in the range 20–35 K.

HoFe$_4$Ge$_2$ displays a re-entrant structural transition [6,7]. The magnetic phase diagram comprises two structural transitions and three magnetic transitions with the wave vectors ($\mathbf{q}_{1o}$, $\mathbf{q}_{2o}$, $\mathbf{q}_{1t}$). The vector subscripts are: o is the orthorhombic and t the tetragonal symmetry. Two magnetic transitions occur simultaneously with the structural changes at $T_N, T_c = 52$ K and $T_c, T_{ic1} = 15$ K. The third is purely magnetic at $T_{ic2} = 40$ K. The first transition is of *second order* while the latter two of *first order*. The sequence of phases follows the path:

$$P4_2/mnm(HT):\ T_N, T_c = 52\,K \rightarrow Cmmm(IT):$$
$$(\mathbf{q}_{1o} = (0\,\tfrac{1}{2}\,0), T_{ic2} = 40\,K \Rightarrow \mathbf{q}_{2o} = (0\,q_y\,0)),\ T_{c'},$$
$$T_{ic1} = 15\,K \Rightarrow P4_2/mnm(LT) : \mathbf{q}_{1t} = (0\,\tfrac{1}{2}\,0).$$

The two times larger orthorhombic phase *Cmmm* ($a_o = (a_t - b_t)$, $b_o = (a_t + b_t)$) which dominates the low-temperature range of ErFe$_4$Ge$_2$ and the intermediate range (*IT*) of HoFe$_4$Ge$_2$ is associated with a distortion of the tetragonal angle γ. The magnetic structures described by the wave vectors $\mathbf{q}_{1o}$, $\mathbf{q}_{2o}$ and $\mathbf{q}_{1t}$, where the components are referred to the reciprocal basis of the conventional *Cmmm* cell, correspond to 3D multi-axial moment arrangements. The moments of the two R sites are polarised within the plane $(1\,1\,0)_t$ or $(1\,0\,0)_o$ at an angle of 55° and 43° to the c-axis for Er and almost parallel to b for Ho. The moments of the Fe atoms display a 3D canted arrangement in the R = Er, Ho compounds in contrast to the 2D canted arrangement within the (0 0 1) plane found in the nonmagnetic R = Y compound. Within the plane (0 0 1) the moments of the Fe atoms with the shortest Fe–Fe distances point towards opposite directions while the moments of atoms located at two successive planes are rotated by $\pi/2$. The Fe average ordered moment values in the RFe$_4$Ge$_2$ compounds formed with a magnetic rare earth (R = Er, Ho) at 1.5 K is more than three times larger than for the compound with R = Y. The double symmetry breaking in the ErFe$_4$Ge$_2$ compound most likely originates from the existence of two competing coupling mechanisms

R–*R* and Fe–Fe of similar strength between the magnetic moments and their coupling with the lattice strains.

The isomorphic compound $DyFe_4Ge_2$ was found by high-resolution XRPD (Part I of the present paper) to undergo a single *HT* magnetostructural transition:

$$P4_2/mnm(HT):\ T_N, T_c = 55\,K \rightarrow Cmmm.$$

Two minor anomalies at $T_{ic2} = 45$ K and $T_{ic1} = 28$ K on the thermal variation of the *a* and the *c* lattice constants, respectively, as well as of several structural parameters indicate the interdependence of structural and magnetic changes in the *LT* orthorhombic phase *Cmmm*.

According to previous studies of ^{57}Fe and ^{161}Dy Mössbauer spectroscopy and magnetic measurements in high magnetic fields [2,3], $DyFe_4Ge_2$ orders antiferromagnetically at 65 ± 1 K and has a *c* axis anisotropy. At 4.2 K it displays two field-induced first-order magnetic transitions a strong one at $B_{crit} = 1.6$ T and a second weaker one at $B_{crit} = 6.0$ T. The authors of Ref [2] report a twofold splitting of the Fe site upon magnetic ordering and an average ordered Fe moment value of $0.53\,\mu_B$/Fe atom at 8 K. The ^{161}Dy Mössbauer spectrum at 4.2 K has sharp lines and is explained by a single spectrum [3]. The estimated average ordered moment value of $10.17(4)\,\mu_B$/Dy atom at 4.2 K is larger than the Dy free ion value $gJ\mu_B = 10\,\mu_B$. The present paper focuses on the magnetic properties on the basis of neutron diffraction data and reports on the sequence of magnetic transitions and the corresponding magnetic structures as well as on the interdependence of subtle crystal structure changes associated with the magnetic ordering and the lattice strains as a function of temperature. These results together with the XRPD are summarised on a magnetic phase diagram and compared to the phase diagrams of the presently known isomorphic compounds.

2. Data collection and analysis

Neutron diffraction experiments were carried out in the temperature range 1.5–74 K at the facilities of the Orphée reactor (LLB-Saclay). The data were collected on the G4.1 (800-cell position sensitive detector: PSD) diffractometer using the wavelength of 2.426 Å. The step increment in 2θ was 0.1° The data were collected in the 2θ region 3–83° for a full set of temperatures in the range 1.5–74 K in steps of and at 293 K on heating. The data were analysed with the program *FullProf* [8]. The drawings of magnetic structures have been performed using the program *FullProf Studio* [9]. Results are given in Figs. 1 and 2 and in Tables 1–4.

The neutron diffraction pattern (G4.1 data) collected in the paramagnetic state at 56 K, is shown in Fig. 2a (top part). The refined parameters and *R*-factors ($R_B = 2.3\%$, $R_{wp} = 14.5\%$) given in Table 1 confirm the RFe_4Ge_2 type of structure. As already mentioned in Part I, the anisotropic line broadening due to microstructure effects is strongly affecting the profile refinements and needs to be corrected. The formulation used in Part I for micro-strain is independent of the used wavelength. Therefore the refined micro-strain parameters of the XRPD data were directly implemented as starting parameters in the calculations for each distinct temperature with the G4.1 instrumental resolution parameters. The peak shape corrections used in the refinements led to a decrease of the R_{wp} weighted profile factor by 4%. In agreement with the X-ray findings the powder pattern contains small amounts (2–3%) of α-Fe and the $DyFe_2Ge_2$ type impurity phase that have been included in the refinement.

3. Magnetic ordering

The neutron data analyses in the magnetic ordered state are based on the simulated annealing method of global optimisation as applied for the $HoFe_4Ge_2$ compound in Ref [7]. The structural parameters used in the simulated annealing were those obtained by the XRPD refinements at the same temperature. To a certain extent, the XRPD parameters were also used in the refinements of the neutron diffraction data. The simulated annealing method has shown that the medium resolution data, obtained for this compound, in the G4.1 instrument does not allow to refine all free

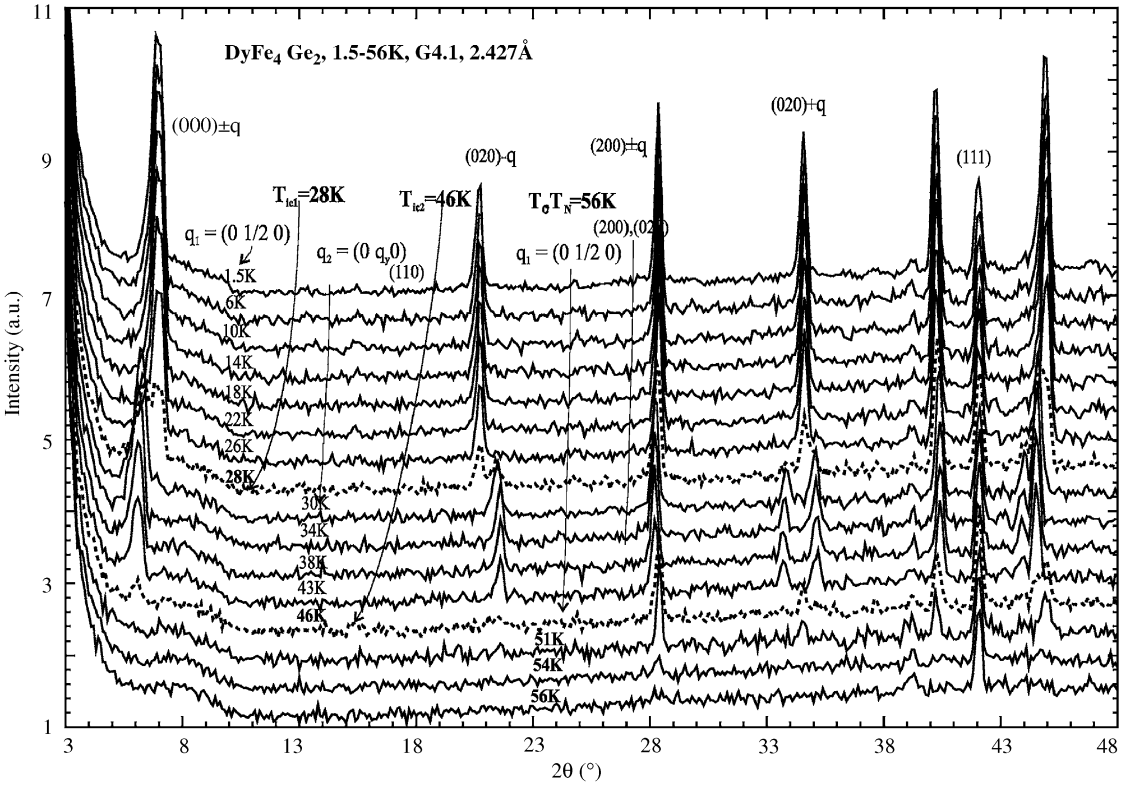

Fig. 1. The low 2θ angle part of the neutron thermo-diffractograms of $DyFe_4Ge_2$, collected (on heating) for various temperatures below the ordering temperature $T_N = 55(2)$ K indicating the interplay magnetic and structural transitions and the re-entrant behaviour of the magnetic wave vector $\mathbf{q}_1 = (0\,\frac{1}{2}\,0)$. The indexing of the nuclear reflections refers to the *Cmmm* ($(a_t\sqrt{2}, a_t\sqrt{2}, c_t)$ cell. The indexing of the magnetic satellites requires the wave vectors $\mathbf{q}_1 = (0\,\frac{1}{2}\,0)$ and $\mathbf{q}_2 = (0\,q_y\,0)$.

parameters. This is the case for the angles of the Fe moment with the *a*-and *c*-axes (Φ and θ respectively). Furthermore, the phases, φ, of the sinusoidal waves of different magnetic sublattices, with respect to the origin, could not be derived in the incommensurate range. All these items were addressed by inserting parameter constraints based on symmetry analysis, on the information from other methods, as Mössbauer and magnetic measurements, and from our own experience with the other isomorphs. It is possible that high-resolution data would provide a better approximation for these parameters as it was the case for $HoFe_4Ge_2$ [7].

3.1. *The wave vectors* $\mathbf{q}_1 = (0\,\frac{1}{2}\,0)$ *and* $\mathbf{q}_2 = (0\,q_y\,0)$

The phase diagram derived in Part (I) comprises two stability ranges of distinct crystal symmetry and one second order *HT* magnetostructural transition at $T_N, T_c = 55$ K. The paramagnetic phase is tetragonal $P4_2/mnm$ while the magnetically ordered phase is orthorhombic, *Cmmm*. The neutron diffraction data collected with a 2 K temperature window for a full set of temperatures will be used to derive the magnetic phase diagram and the corresponding magnetic structures. This requires the detection of the wave vector(s) associated with the magnetic ordering, which is the most important step in the analysis of neutron powder diffraction data [10]. This can be achieved by using the profile matching technique [8] that takes the integrated intensities as free parameters and calculates the position of the Bragg peaks as a function of the lattice constants and propagation vectors. The indexing of the magnetic reflections in a powder pattern is greatly facilitated by low 2θ

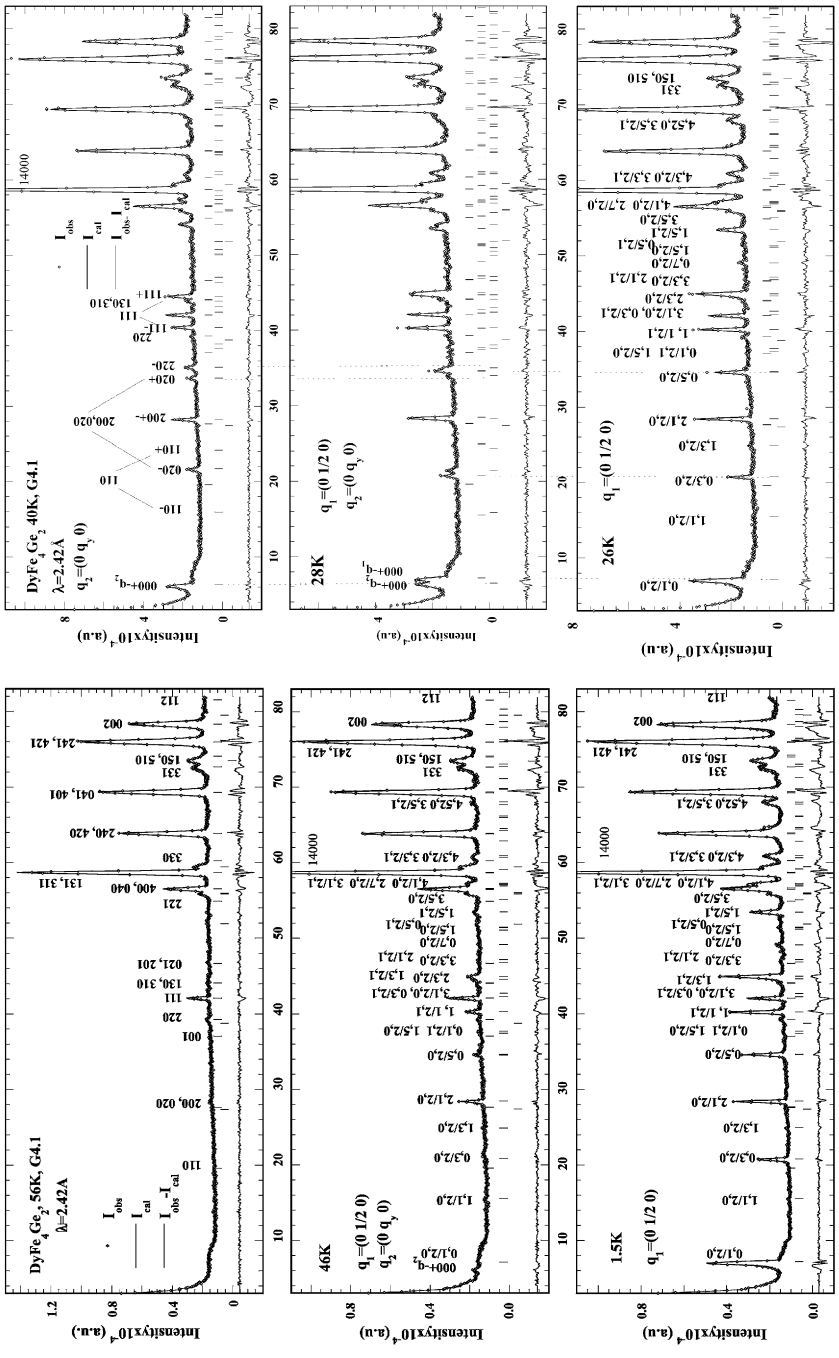

Fig. 2. (a) Observed and calculated (G4.1 instrument) neutron intensities of $DyFe_4Ge_2$ in the paramagnetic state at 56 K (top part) and the magnetically ordered state at 46 K, above the transition commensurate ($\mathbf{q}_1 = (0\frac{1}{2}0)$) $T_{ic2} = 45$ K $\rightarrow$ to incommensurate ($\mathbf{q}_2 = (0\,q_y\,0)$) state and at the lowest temperature 1.5 K below the lock-in transition at ($\mathbf{q}_2 = (0\,q_y\,0)$, $T_{ic1} = 28$ K $\rightarrow$ ($\mathbf{q}_1 = (0\frac{1}{2}0)$). Both phases are described by the commensurate wave vector $\mathbf{q}_1 = (0\frac{1}{2}0)$. The indexing refers to the orthorhombic *Cmmm* phase. (b) Observed and calculated (G4.1 instrument) neutron intensities of $DyFe_4Ge_2$ in the magnetically ordered state at (a) 40 K below the transition $T_{ic2} = 45$ K where the system becomes incommensurate with the crystal lattice $\mathbf{q}_2 = (0\,q_y\,0)$ (top part) (b) at the lock-in first-order transition temperature $T_{ic1} = 28$ K with coexisting phases $\mathbf{q}_1 = (0\frac{1}{2}0)$ and $\mathbf{q}_2 = (0\,q_y\,0)$ and (c) at 26 K, just below T_{ic1}, in the commensurate $\mathbf{q}_1 = (0\frac{1}{2}0)$ phase. The indexing refers to the orthorhombic *Cmmm* phase.

Table 1
Refined structural parameters of $DyFe_4Ge_2$ neutron diffraction data (G4.1) in the paramagnetic state at 56 K and in the magnetically ordered state at 46, 40, 28, 26 and 1.5 K

$P4_2/mnm$ atom/site	$P4_2/mnm$ 56 K			*Cmmm* 56 K			46 K		40 K		28 K		26 K		1.5 K	
	x	y	z	Atom site	x	y	x	y	x	y	x	y	x	y	x	y
Dy:2*b*																
1	0	0	$\frac{1}{2}$	Dy1: 2*d*	0	0	0	0	0	0	0	0	0	0	0	0
2	$\frac{1}{2}$	$\frac{1}{2}$	0	Dy2:2*b*	$\frac{1}{2}$	0	$\frac{1}{2}$	0	$\frac{1}{2}$	0	$\frac{1}{2}$	0	0.5	0.0	0.5	0.0
Fe: 8*i* $(x, y, 0)$	0.0946(4)	0.3532(5)	0	Fe1: 8*p*	0.1293(9)	0.2239(4)	0.1321	0.2296	0.1322	0.2281	0.1322	0.2281	0.1322	0.2281	0.1322	0.2281
$(\frac{1}{2}+y, \frac{1}{2}-x, \frac{1}{2})$	0.8532(2)	0.4054(2)	$\frac{1}{2}$	Fe2: 8*q*	0.2761(4)	0.1293(9)	0.2787	0.1266	0.2781	0.1286	0.2781	0.1286	0.2781	0.1286	0.2781	0.1286
Ge:4*g* $(x, -x, 0)$	0.2141(1)	−0.2141(1)	0	Ge1: 4*g*	0.2141(8)	0	0.2164	0	0.2157	0	0.2157	0	0.2156	0	0.2157	0
$(x+\frac{1}{2}, x+\frac{1}{2}, \frac{1}{2})$	0.7141(1)	0.7141(1)	$\frac{1}{2}$	Ge2: 4*j*	0	0.2859(8)	0	0.2828	0	0.2828	0	0.2828	0	0.2828	0	0.2828
a (Å)	7.2989(2)			10.3223(3)			10.3295(13)		10.3307(11)		10.3361(7)		10.3368(6)		10.3339(6)	
b (Å)	7.2989(2)			10.3223(3)			10.3127(12)		10.3138(10)		10.3063(7)		10.3055(6)		10.3048(6)	
a/*b*	1			1			1.00163		1.00164		1.0029		1.00304		1.00331	
c (Å)	3.8609(1)			3.8609(1)			3.8603(1)		3.85367(3)		3.8604(7)		3.8604(1)		3.8612(1)	
V/*l* (Å^3)	205.690(1)			411.380(2)			411.23(7)		411.25(6)		411.24(4)		411.23(4)		411.18(4)	
R_B,R_{wp},R_{exp} (%)	4.7, 14, 7						5, 16, 7.3		5, 15.7, 7.2		4.8, 15.4. 7		4.8, 15, 7		9, 14, 5	

The refined parameters of the 56 K tetragonal phase $P4_2/mnm$ are also given in the orthorhombic setting *Cmmm* for comparison reasons with the *LT* phases. The overall temperature factor B (Å^2) is fixed to the 0.27. R_B, R_{wp} and R_{exp} (%) are: the Bragg, the weighted profile and the expected reliability factors.

Table 2a
Irreps for $\boldsymbol{q} = (0\ q_y\ 0)$ in *Cmmm*

	E	2_y	m_z	m_x
Γ	1	1	1	1
Γ_2	1	1	−1	−1
Γ_3	1	−1	1	−1
Γ_4	1	−1	−1	1

angle observations within the first Brillouin zone as this derives straightforwardly the modulus of the wave vector.

The low 2θ angle part of the neutron thermodiffractogram in the temperature range 1.5–56 K (G4.1 instrument) c.f. Fig. 1, displays a large number of additional peaks of magnetic origin with a rather complex topology and temperature-dependent positional and intensity changes. The magnetic contributions occur at reciprocal lattice positions other than the nuclear reflections ($\mathbf{q} \neq 0$). Ferromagnetism can be ruled out from the absence of any intensity enhancement at the positions of nuclear reflections i.e. (1 1 0) and (1 1 1) and (2 0 0)/(0 2 0) at about $2\theta \approx 20^\circ$, 42° and 48°, respectively, (Figs. 1 and 2). In conjunction with the results of Part I it is evident that long range magnetic order sets in for $T < 56$ K and that the magnetic phase diagram comprises at least three ranges of distinct magnetic ordering including the paramagnetic state.

Fig. 3 points out in more detail the major experimental facts by following the very different thermal variation of the position and the integrated neutron intensity of the first few magnetic peaks occurring around 2θ: 7°, 21° and 28°. The latter peak at $2\theta \approx 28^\circ$ (Fig. 3(c)) on the right side of the (2 0 0)/(0 2 0) position becomes already visible below 55 K and persists over the entire magnetically ordered regime. Its integrated intensity and 2θ position do not vary smoothly with temperature. As no other magnetic reflections are visible at higher temperatures, the temperature $T_N = 55$ K marks the transition from the paramagnetic to the magnetic ordered state.

The most characteristic observation in Fig. 3(c) is the re-entrant jump of the reflection angle $2\theta \approx 28^\circ$ at the temperatures of $T_{ic2} = 45$ K and

Table 2b
Split of the atomic positions under the action of the wave vector $\mathbf{q} = (0\, q_y\, 0)$ in the *Cmmm* space group (without $(\frac{1}{2}\frac{1}{2}0)$ centring) see Fig. 12

Site/atom		*Cmmm*				*Cmmm* $\mathbf{q} = (0\, q_y\, 0)$ magnetic						
	No.	x	y	z	No.	x	y	z	No.	x	y	z
Dy 2*d*	1	0	0	$\frac{1}{2}$	1	0	0	$\frac{1}{2}$	—			
Dy 2*b*	2	$\frac{1}{2}$	0	0	2	$\frac{1}{2}$	0	0	—			
Fe 8*p*	1_1	x	y	0	1_1	x	y	0	1_2	$-x$	y	0
	2_1	$\frac{1}{2}-x$	$\frac{1}{2}-y$	0	2_1	x	y	0	2_2	$-x$	y	0
Fe 8*q*	3_1	x	y	$\frac{1}{2}$	3_1	x	y	$\frac{1}{2}$	3_2	$-x$	y	$\frac{1}{2}$
	4_1	$\frac{1}{2}-x$	$\frac{1}{2}-y$	$\frac{1}{2}$	4_1	x	y	$\frac{1}{2}$	4_2	$-x$	y	$\frac{1}{2}$

Part (I). The Fe 8*p* site (orbit 1, red) splits in to orbits →I (Fe1$_i$) and II (Fe2$_i$) and Fe 8*q* (orbit 2, green), in to orbits →III (Fe$_{3i}$) and IV (Fe$_{4i}$). Dy occupies the 2*b* (Dy1) and 2*d* (Dy2) sites. The atoms of the Fe orbits are labelled by the numbers 1_i, 2_i, 3_i, 4_i where $i = 1-4$, thus four Fe atoms with the same i belong to the same Fe tetrahedron.

Table 3
Fourier components $\mathbf{S_q} = \frac{1}{2}(u,\, v,\, w)$ of the six magnetic sublattices (orbits), without centring translation $(\frac{1}{2}\frac{1}{2}0)$, of DyFe4Ge2 for the four representations associated with the wave vector $\mathbf{q} = (0q_y, 0)$ referring to the *C*-cell (Figs. 11a–c)

Site	Atom	x	y	z	Γ_1	Γ_2	Γ_3		Γ_4		$\Gamma_2+\Gamma_3$		
					w	u	v	w	u	v	u_o	v_o	w_o
1	Dy1	0	0	0.5			v_1	w_1	u_1			7.1(4)	4.7(3)
2	Dy2	0.5	0	0			v_2	w_2	u_2			8.8(4)	5.8(3)
3	Fe1$_1$	0.1322	0.2281	0	w_3	u_3	v_3	w_3	u_3	v_3	−1.9(3)	1.1(3)	−1.1(2)
	Fe1$_2$	0.8678	0.2281	0	$-w_3$	$-u_3$	v_3	w_3	u_3	$-v_3$	1.9(3)	1.1(3)	−1.1(2)
4	Fe2$_1$	0.3678	0.2718	0	w_4	u_4	v_4	w_4	u_4	v_4	2.0(2)	−0.9(1)	−1.1(2)
	Fe2$_2$	0.6312	0.2718	0	$-w_4$	$-u_4$	v_4	w_4	u_4	$-v_4$	−2.0(2)	−0.9(1)	−1.1(2)
5	Fe3$_1$	0.2781	0.1286	0.5	w_5	u_5	v_5	w_5	u_5	v_5	3.1(2)	−1.4(1)	0.1(2)
	Fe3$_2$	0.7219	0.1286	0.5	$-w_5$	$-u_5$	v_5	w_5	u_5	$-v_5$	−3.1(2)	−1.4(1)	0.1(2)
6	Fe4$_1$	0.2218	0.3714	0.5	w_6	u_6	v_6	w_6	u_6	v_6	3.0(2)	1.7(4)	0.1(2)
	Fe4$_2$	0.7792	0.3714	0.5	$-w_6$	$-u_6$	v_6	w_6	u_6	$-v_6$	3.0(2)	1.7(4)	0.1(2)

The amplitudes (u_0, v_0, w_0) are the refined parameters at 1.5 K for **q**1 for $\Gamma_2+\Gamma_3$. The coordinates of the atoms Fe1$_i$ and Fe2$_i$ pertaining to the orbits, $i = 1, 2$ are (x_i, y_i, 0), $(1-x_i, y_i, 0)$ respectively and those of Fe3$_i$ and Fe4$_i$ (x_i, y_i, $\frac{1}{2}$), $(1-x_i,\, y_i,\, \frac{1}{2})$.

$T_{ic1} = 28$ K. In the T_{ic2}~T_N range the peak position remains within error unchanged while its intensity increases continuously with decreasing temperature. At $T_{ic2} = 45$ K one observes a discontinuous positional change towards lower angles and a 20% intensity decrease. On further cooling the 2θ angle decreases down to 38 K and after a strong upturn increases slowly down to $T_{ic1} = 28$ K where it jumps to higher angles and approaches its *HT* original position. The magnetic peaks at $2\theta \approx 7^\circ$ and 21° shown in Figs. 3(a) and (b) respectively, appear just below $T_{ic2} = 45$ K. Their intensities increase with decreasing temperature and display in a similar manner a discontinuity at $T_{ic1} = 28$ K while their positions jump in opposite directions the first peak within the first Brillouin zone $(0\,0\,0)\pm\mathbf{q}$ to higher angles and the second $(0\,2\,0)-\mathbf{q}$ to lower angles. Below 28 K their position remains unchanged. This behaviour is compatible with a wave vector confined to the *b*-axis as already found in the Er and Ho compounds. The reflection at the right side of the $(2\,0\,0)/(0\,2\,0)$ nuclear peak corresponds to the $(2\,0\,0)\pm\mathbf{q}$ satellite. The temperature dependent

Table 4
Refined magnetic parameters of $DyFe_4Ge_2$ at various temperatures from G4.1 neutron data

DyFe4Ge2 *Cmmm*	1.5 K $\mathbf{q}_1 = (0\frac{1}{2}0)$	26 K $\mathbf{q}_1 = (0\frac{1}{2}0)$	28 K $\mathbf{q}_1 = (0\frac{1}{2}0)$	28 K $\mathbf{q}_2 = (0, 0.449, 0)$	40 K $\mathbf{q}_2 = (0, 0.4339, 0)$	46 K $\mathbf{q}_1 = (0\frac{1}{2}0)$
Dy1: 2*d* (0, 0, 1/2)						
μ_y, $\mu_z(\mu_A)$	7.1(4), 4.7(3)	6.6(4), 4.0(3)	4.5(4), 2.6(2)	3.9(4), 2.1(3)	4.9(6), 2.8(3)	4.8(2), 0
$\mu_T(\mu_B)$, $\Phi, \theta(^\circ)$	8.5(5), 90, 57(1)	7.7(7), 90, 59(1)	5.2(7), 90, 60(1)	4.3(5), 90, 60(2)	5.7(6), 90, 59(2)	4.8(2), 90, 90
Dy2: 2*b* (1/2, 0, 0)						
μ_y, $\mu_z(\mu_A)$	8.8 (4), 5.8(3)	8.0(4), 4.8(3)	6.1(4), 3.4(4)	5.4(4), 3.0(3)	6.6(6), 3.9(4)	4.8(2), 0
$\mu_T(\mu_B)$, $\Phi, \theta(^\circ)$	10.6(5), 90, 57(1)	9.4(5), 90, 59(1)	9.4(5), 90, 60(1)	6.2(5), 90, 60(2)	7.7(7), 90, 59(2)	4.8(2), 90, 90
Fe1:8*p*(x, y, 0) at						
μ_x, μ_y, $\mu_z(\mu_A)$	−1.9(3), 1.1(3), 1.1(2)	−2.0(4), 0.4(6), 1.0(1)	−1.8(2), 0.1(3), −0.7(1)	−1.8(2), 0.1(3), 0.7(1)	−1.8(3), 1.2(4), −1.0(1)	−1.3(3), −0.5(3), 0
$\mu_T(\mu_B)$, $\Phi, \theta(^\circ)$	2.5(2), 151(7), 116(4)	2.3(3), 168(17), 117(5)	2.0(1), 175(8), 112(4),	2.0(1), 175(9), 112(4)	2.4(2), 146(11), 116(4)	1.4(2), 203(15), 90
Fe2:8*p*(1/2 − *x*, 1/2 − *y*, 0)						
μ_x, μ_y, $\mu_z(\mu_A)$	2.0(2), −0.9(1), 1.1(2)	1.9(4), −0.7(5),1.0(1)	1.7(4), −0.7(1), −0.7(1)	1.8(2),0.7(5),1.0(1)	1.9(4), −0.9(3), −1.0(1)	−0.3(4), −1.3(3), 0
$\mu_T(\mu_B)$, $\Phi, \theta(^\circ)$	2.5(2), 337(1), 116(4)	2.3(3), 340(11), 117(5)	2.0(1), −22(6), 112(4)	2.0(1), 22(6), 112(2)	2.4(2), −26(8), 116(4)	1.4(2), −103(19),90
Fe3:8*q*(x, y, 1/2) at						
μ_x, μ_y, $\mu_z(\mu_A)$	3.2(2), −1.4(1), −0.1(2)	2.6(2), −1.3(3), 0	1.8(2), −0.7(2), 0	1.8(2), −0.7(2), 0	2.1(2), −1.0(3), 0	−0.3(4), −1.3(3), 0
$\mu_T(\mu_B)$, $\Phi, \theta(^\circ)$	3.5(2), 337(1), 88(4)	2.9(2), 333(7), 90	2.0(1), −22(6), 90	2.0(1), −22(6), 90	2.4(2), −26(8), 90	1.4(2), −103(19), 90
Fe4:8*q*(1/2 − *x*, 1/2 − *y*, 1/2)	−3.2(2), 1.7(4), −0.1(2)					
μ_x, μ_y, $\mu_z(\mu_A)$	3.5(2), 151(7), 88(4)	−2.7(2), 0.9(5), 0	−2.0(2), 0.2(3), 0	−2.0(2), 0.1(3), 0	−2.0(3), 1.3(4), 0	−1.3(2), −0.5(3), 0
$\mu_T(\mu_B)$, $\Phi, \theta(^\circ)$		2.9(2), 160(10), 90	2.0(1), 175(8), 90	2.0(1), 175(9), 90	2.4(2), 146(12), 90	1.4(2), 203(15), 90
R_B, R_m, R_{m2} (%)	9, 9,	5, 8.5	5, 12, 13		5, −, 12	5, 15,−,
R_{wp} (%), R_{exp} (%)	14, 4.6	15, 7	15, 7		15, 7	16, 7

μ_x, μ_y, μ_z, μ_T are the moment components (Fourier coefficients) of the Dy and Fe sublattices Φ and θ, are the moment angles with the *a*, *c* axes. R_B, R_{m1} and R_{m2} (%), are the Bragg *R*-factors of the nuclear and magnetic phases associated with ($\mathbf{q}_1$ or $\mathbf{q}_2$) involving integrated intensities; and R_B, R_{wp}, R_{exp} (%) are: the Bragg, the weighted and the expected profile reliability factors.

positional shifts of the magnetic reflections would then correspond to changes of the wave vector length with temperature.

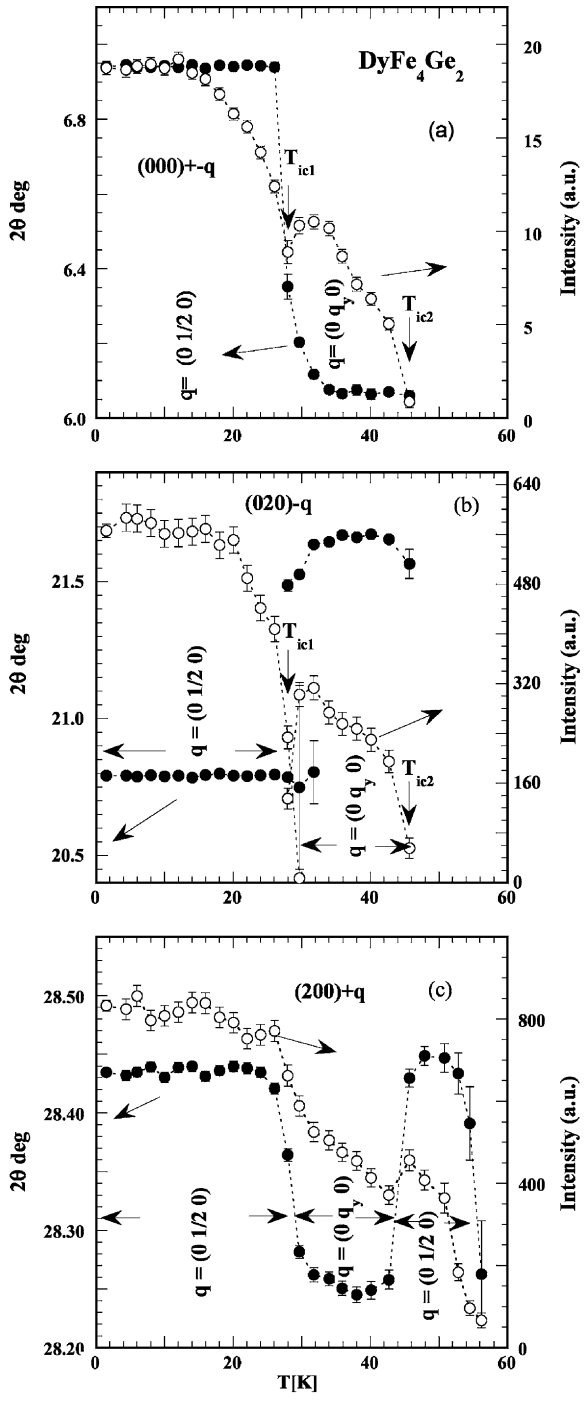

Fig. 3. Temperature dependence of the $DyFe_4Ge_2$ magnetic neutron intensity of the well-resolved satellites at low 2θ angles of the commensurate and incommensurate phases: (a) the zero point satellites $(0\,0\,0)\pm\mathbf{q}_i$: $(0\pm q_y\,0)$, $(0\,\frac{1}{2}\,0)$ (b) the $(0\,2\,0)-\mathbf{q}_i$satellites: $(0\,2\overline{q}_y\,0)$ $(0\,\frac{3}{2}\,0)$ and (c) the $(2\,0\,0)\pm\mathbf{q}_i$ satellites: $(2\pm q_y\,0)$, $(2\,\frac{1}{2}\,0)$. The changes of the 2θ angle, and the stability regions of the corresponding crystal and magnetic structures with the wave vectors $\mathbf{q}_1$, $\mathbf{q}_2$ resulting from the refinements, are also shown. The interplay between the wave vectors and the re-entrant behaviour of the commensurate phase is best seen in the (bottom part). The dotted line is a guide for the eye.

Profile matching at various temperatures led to the wave vectors: $\mathbf{q}_1 = (0\,\frac{1}{2}\,0)$ and $\mathbf{q}_2 = (0\,q_y\,0)$ that explain all observations at any given temperature. The $\mathbf{q}_2 = (0\,q_y\,0)$ vector has a temperature dependent length and is restricted to the intermediate temperature range $T_{ic1} = 28\,\mathrm{K} \leqslant T \leqslant T_{ic2} = 45\,\mathrm{K}$ where the magnetic lattice becomes incommensurate with the crystal lattice.

Once the wave vectors of a magnetic phase are known symmetry analysis may be used to develop a magnetic structure model and insert several parameter constraints in the refinements of the neutron diffraction data.

3.2. Irreducible representations of the propagation vector group $G_{\mathbf{q}}$ for $\mathbf{q} = (0\,q_y\,0)$ in Cmmm

The present analysis is common for both the commensurate $\mathbf{q}_1 = (0\,\frac{1}{2}\,0)$ and the incommensurate $\mathbf{q}_2 = (0\,q_y\,0)$ magnetic phases. The propagation vector $\mathbf{q} = (0\,q_y\,0)$ is located at the interior of the Brillouin Zone and its star has two arms $\{\mathbf{q}, -\mathbf{q}\}$. The group of the propagation vector is $G_{\mathbf{q}} = Cm2\,m = \{E, 2_y, m_z, m_x\}$. There are four real irreducible representations (Irreps) of dimension 1 as given in Table 2a.

Under the action of the wave vector $\mathbf{q} = (0\,q_y\,0)$ in the parameter space of the *Cmmm LT* structure the two Fe sites split in the following way: the Fe 8*p* site (orbit 1, red colour in Fig. 7b (see also Fig. 12 of Part (I)) splits into the orbits $\rightarrow$I($Fe1_i$) and II ($Fe2_i$) and the Fe 8*q* site (orbit 2, green colour), into the orbits $\rightarrow$III (Fe_{3i}) and IV (Fe_{4i}). Each orbit comprises now four atoms including the *C*

translation. Dy occupies the 2*b* (Dy1) and 2*d* (Dy2) sites. The total number of sites has increased from four to six. The atoms of the Fe orbits are labelled by the numbers j_i, ($j = 1,4$ and $i = 1,4$): 1_i, 2_i, 3_i, 4_i in Fig. 7b. In this way four Fe atoms with different j and the same i belong to the same Fe tetrahedron.

The atomic and magnetic parameters and magnetic modes are summarised in Table 3 for the *LT* lock-in phase at 1.5 K for the atoms within the primitive cell, the moment of atoms related by the centring translation $\mathbf{t} = (\frac{1}{2}\frac{1}{2}0)$ is obtained by multiplying the moment of initial atoms by the phase factor $\exp\{-2\pi i\mathbf{q}.\mathbf{t}\}$. The structural and magnetic parameters for various temperatures are given in Tables 1 and 4, respectively.

Symmetry analysis shows that the decomposition of the global magnetic representation Γ_m in the Irreps is the same for the two Dy sites and the same for all Fe sites: $\Gamma_m = \Gamma_2 + \Gamma_3 + \Gamma_4$ (Dy sites) and $\Gamma_m = \Gamma_1 + 2\Gamma_2 + \Gamma_3 + 2\Gamma_4$ (Fe sites). The Fourier coefficients deduced from the basic functions are given for each Irrep. The coefficients (*u*, *v*, *w*) are, in principle different for each site but the magnetic modes are the same for all Fe orbits for the corresponding Irreps. Dy may have only uniaxial structures. For the Fe sites Table 3 shows that the Γ_1 and Γ_3 representations allow only *w* Fourier components, while Γ_2 and Γ_4 allow *u* and *v* components.

3.3. Magnetic structures

3.3.1. The LT commensurate phase: $\mathbf{q}_1 = (0\frac{1}{2}0)$ and $\Gamma_2 + \Gamma_3$ Irreps

As can be seen in Table 3 the direction of the Dy moments due to their high-symmetry position, is constrained to one of the orthorhombic mirror planes m_x, m_y, m_z. The Dy atoms may have a single-moment component, which is perpendicular to any of the mirror planes. Each of the four Fe orbits comprises two atoms related by the mirror operation across the plane m_x. The moment components of the atom pairs belonging to the same orbit are symmetry related. For instance, in the Γ_2 representation allowing (*u*, *v*) components the atoms $Fe1_1$ and $Fe1_2$ of the first orbit have the same moment components v_o ((+ +) mode for m_y components), parallel to the anti-mirror plane m'_x but opposite sign for the u_o component perpendicular to that plane ((+ −) mode for m_x components). These and similar parameter constraints were used throughout the refinements depending on the model selected for each region of the phase diagram.

The refinements indicated that the *LT* magnetic structure with $\mathbf{q}_1 = (0\frac{1}{2}0)$ could not be described by a single representation and its description requires a mixture of the representations Γ_2 and Γ_3 for all magnetic sites. This corresponds to a lowering of the magnetic symmetry to monoclinic and to an increase of the number of free parameters. The mirror plane m_x has negative character in both representations: it becomes an anti-mirror plane m'_x. The refined Fourier components (u_o,v_o,w_o) at 1.5 K for all atoms are given in Table 3. The refined parameters at the upper end of the stability range of the *LT* lock-in phase at 26 K show a reduction of the moment values due to increasing thermal disorder but not essential changes see Table 4 and Fig. 6(a).

The 1.5 K refined parameters led to a 3D canted arrangement (Fig. 7a) of the Fe moments with eight sublattices and two sublattices for Dy, similar to the *LT* arrangement found in the $HoFe_4Ge_2$ [7] compound. In Fig. 7a we show the twice enlarged cell along *b* where the global phase of $\Phi_o = -\pi/4$ has been used in order to obtain equal moment values but a different sign for all atoms of the same orbit related by the translation $(\frac{1}{2}\frac{1}{2}0)$ and the anti-translation $(0\frac{1}{2}0)$. The sign change of four translationally equivalent atoms i.e. Dy1 (Dy2) along the diagonals $(1 \pm 1\,0)$ follows the pattern (+ − − +). The ordered moment values obtained from the Fourier coefficients using the global phase $\Phi_o = -\pi/4$ for Dy1 is: $8.5 \times \cos(2\pi\mathbf{q}\mathbf{R}_n - \pi/4) = 6.0(4)$ and $7.5(2)\,\mu_B$ for Dy2. The moments are reduced relatively to the data reported in [3] by Mössbauer measurements and also relatively to the free ion value for Dy^{3+}, $gJ(\mu_B) = 10(\mu_B)$ presumably due crystal field effects. The moments of both Dy sites are making an angle of $\theta = 57^\circ(4)$ with the *c* axis. Similar angles were found in $ErFe_4Ge_2$ of 55° and 42° respectively. The moment values of Fe1 and Fe2 sublattices are equal to $1.8(2)\,\mu_B$ and those of the

Fe3 and Fe4 sublattices are equal to 2.4(2) μ_B. They compare very well with the corresponding values of 2.4 and 1.4 μ_B found in $ErFe_4Ge_2$ and 1.8 μ_B for $HoFe_4Ge_2$. Here we would like to note that all moment values given in Ref [7] for $HoFe_4Ge_2$ have to be multiplied by 2. This error was due to a mistake we made putting incorrect occupation numbers in the magnetic phase.

3.3.2. The HT commensurate phase: $\mathbf{q}_1 = (0\,\frac{1}{2}\,0)$ *and* Γ_2 *Irrep*

All magnetic peaks for $T > T_{ic2} = 45$ K were indexed using the wave vector $\mathbf{q}_1 = (0\,\frac{1}{2}\,0)$. A small peak at $2\theta \sim 6^\circ$ visible in Fig. 2a (middle part) corresponds to the zero point satellite of a coexisting small amount of the incommensurate phase $\mathbf{q}_2 = (0\,q_y\,0)$ at 46 K just above the first order transition at $T_{ic2} = 45$ K indicating the first order character of the transition. No attempt was undertaken to refine the coexisting phase as no other peaks could be found. All refinements undertaken in the *HT* stability range of the commensurate phase $T_{ic2} = 45\,\mathrm{K} - T_N$ were not sensitive to the angle θ between moment and the *c* axis. Furthermore one observes that the zero point satellite: $(0\,\frac{1}{2}\,0)$ and the $(0\,2\,0) - q_y = (0\,\frac{3}{2}\,0)$ satellite vanish above T_{ic2}.

This indicates that the Dy moments point along the direction of the wave vector *b*. m_z components would contribute to the magnetic intensities and m_x components are not allowed by symmetry for Dy see Table 3. The Fe sites may have only m_{xy} components. The m_z Fe components with $(++)$ mode in the Γ_3 representation found at *LT* would contribute to the magnetic $(0\,\frac{1}{2}\,0)$ intensity. The m_x components, with the same contribution to the magnetic structure factor and opposite sign $((+-)$ mode) cannot contribute to the $(0\,\frac{1}{2}\,0)$ intensity.

In the 46 K refinements given in Table 4 for the *HT* lock-in phase $\mathbf{q}_1 = (0\,\frac{1}{2}\,0)$ all moments were therefore constrained to the (0 0 1) plane ($\theta = 90^\circ$ see Fig. 7b). In fact this model corresponds to the representation Γ_2. The amplitude of the refined Fourier coefficients of all Fe sublattices equal 1.4(2) μ_B and the ordered moment value, using an overall phase factor of $-\pi/4$, gives $1.4 \times \cos(\pi/4)\,\mu_B$ that equals 1 μ_B/Fe atom. The magnetic moments of the Fe atoms located at the corners of a compact tetrahedron, have a planar canted arrangement but a different one from that found in the orthorhombic (*Pnnm*) YFe_4Ge_2 at 1.5 K [1] where the mutual moment direction of the atom pairs belonging to the same orbit (Fe1, Fe2) and (Fe3, Fe4) are anti-parallel but point to perpendicular directions restoring the local tetragonal symmetry.

The imposed parameter constrains in $DyFe_4Ge_2$ led to a 2D model for the *HT Cmmm* $\mathbf{q}_1$ magnetic phase with a ferrimagnetic moment arrangement within the Fe compact tetrahedra with the moments of the atom pairs ($Fe1_1$ and $Fe4_1$) and of ($Fe2_1$ and $Fe3_1$) in parallel and canted relatively to the Dy moments. Antiferromagnetism is then conserved by *C* centring and the antitranslation along *b* (see Fig. 7(b)). The ordered moment values for Dy1 and Dy2 at 46 K using the global phase factor $\pi/4$ is 3.4(2) μ_B. The Dy moments point along the *b*-axis in agreement with the representation Γ_2. As already said, the refinements were not sensitive to the angles of the Fe moment with the *a*- and *c*-axes. According to the present results the *HT* lock-in phase has a collinear Dy and a planar Fe moment arrangement. Our results concerning the in plane Fe moment angles depend also on the imposed constraints which have to be verified by high resolution neutron data. Therefore, the kind of spin reorientation from the 3D *LT* lock-in $\rightarrow$2D *HT* lock in structure has to be seen with some caution.

3.3.3. The incommensurate magnetic phase: $\mathbf{q}_2 = (0\,q_y\,0)$ *and* $\Gamma_2 + \Gamma_3$ *Irreps*

The 28 K data could be only indexed assuming two coexisting phases in form of domains with a commensurate $\mathbf{q}_1 = (0\,\frac{1}{2}\,0)$ and an incommensurate $\mathbf{q}_2 = (0\,q_y\,0)$ wave vector. The number of orbits is the same for the two phases but the number of free parameters increases as the phases between the atoms are not fixed by symmetry as for the commensurate case.

Once the moment components (Fourier coefficients) within the orthorhombic cell are defined the magnetic moment direction of any translationally equivalent atom may be calculated. The magnetic moment value $\boldsymbol{\mu}_{nj}$ of the *j*th atom in the *n*th cell at

position $\mathbf{R}_n$, is given by the relation

$$\boldsymbol{\mu}_{nj} = \sum_{\{\mathbf{q}\}} \mathbf{S}_{\mathbf{q}j} \exp\{-2\pi i \mathbf{q}\mathbf{R}_n\} = \sum_{1/2\{\mathbf{q}\}} [\mathbf{R}_{\mathbf{q}j} \cos\{2\pi(\mathbf{q}\mathbf{R}_n + \varphi_{\mathbf{q}j})\} + \mathbf{I}_{\mathbf{q}j} \sin\{2\pi(\mathbf{q}\mathbf{R}_n + \varphi_{\mathbf{q}j})\}], \quad (1)$$

where the general Fourier coefficients are:

$$\mathbf{S}_{\mathbf{q}j} = \tfrac{1}{2}\{\mathbf{R}_{\mathbf{q}j} + i\mathbf{I}_{\mathbf{q}j}\} \exp\{-2\pi_i \varphi_{\mathbf{q}j}\} = \mathbf{S}^*_{-\mathbf{q}j}. \quad (2)$$

For a sinusoidal modulated structure (single pair $\mathbf{q}$,$-\mathbf{q}$ and $\mathbf{I}_{\mathbf{q}j} = 0$, $\boldsymbol{R}_{\mathbf{q}j} = \mu_{oj} z$) this expression is

$$\boldsymbol{\mu}_{nj} = \mu_{oj} \mathbf{z} \cos(2\pi \mathbf{q} \cdot \mathbf{R}_n + \varphi_j), \quad (3)$$

where μ_{oj} is the amplitude of the moment, $\varphi_{\mathbf{q}j}$ (or φ_j) is the phase relative to the origin, and $\mathbf{z}$ is a unit vector along the moment direction. The results given in Table 4 are from a simultaneous refinement of both phases for the $\mathbf{q}_2 = (0\, \mathrm{q}_y\, 0)$ incommensurate orthorhombic phase with $\mathrm{q}_y = 0.449(1)$ at 28 K refer also to the same *C*-cell. The simplest possible model is that of a multi-axial sine wave modulated structure as shown in Fig. 7c for 40 K. The starting parameters for the sine wave model were those obtained by the simulating annealing method. However, the data were insensitive to some of the parameters indicating the existence of strong parameter correlations. Convergence was achieved similarly to the *HT* range using the following constraints: (i) the Dy and Fe moments to the same values, respectively (ii) the relative phases of the atoms arbitrary to $\varphi = \pm\pi/4$ as in the *HT* $\mathbf{q}_1$ phase (iii) the moment angle θ with the *c* axis of the Fe orbits with the same *z* coordinate as ((Fe1$_i$ and Fe2$_i$) at $z = 0$, (Fe3$_i$ and Fe4$_i$) at $z = 1/2$) to the same value (iv) the in-plane moment angles Φ with the *a* axis to the same value for atom pairs (Fe1$_i$–Fe4$_i$) and (Fe2$_i$–Fe3$_i$). It is to note that similar constraints were applied in the $HoFe_4Ge_2$ refinements supported by simulated annealing. The reliability factors $R_B = 5\%$, $R_{wp} = 15\%$ and $R_{m1} = 12\%$, $R_{m2} = 13\%$ show a satisfactory agreement between calculated and observed data for both phases.

In the incommensurately modulated structure the moment of each sublattice has a distinct orientation but different from that found in the commensurate phases as can be seen in Fig. 7(c) for a few cells.

The thermal variation of the moment amplitudes Fig. 6(a) shows a discontinuity at 28 K due to the coexistence of the $\mathbf{q}_1$ and $\mathbf{q}_2$ phases indicating that the *LT* lock-in transition is of first order. The average moment amplitude in this range is $\sqrt{(m_1^2 + m_2^2)}$ where m_1 and m_2 the refined values pertaining to the two vectors (see Fig. 6(a)) i.e. the calculated value for Dy(1) is 6.7 μ_B/atom which fits very well in the curve.

3.4. Re-entrant first-order magnetic transitions at $T_{ic1} = 28$ K and $T_{ic2} = 45$ K

The thermal variation of the diffraction angle of several magnetic reflections can be reproduced by following the variation of the wave vector and the lattice parameters with temperature. Fig. 4 depicts the changes of the lattice parameters at the Néel *HT* transition temperature $T_{N,c} = 55$ K and at the *LT* transition at $T_{ic1} = 28$ K. The former is characterised by drastic increase of the $a/b > 1$ ratio or the shear strain $e_{xy} \approx 2(a-b)/(a+b)$ and the latter by changes of the *b*- and *c*-axes in opposite directions while *a* remains unchanged, see also Part I. Small differences in the absolute lattice parameter values between the two measurements are due to uncertainty of the neutron wavelength.

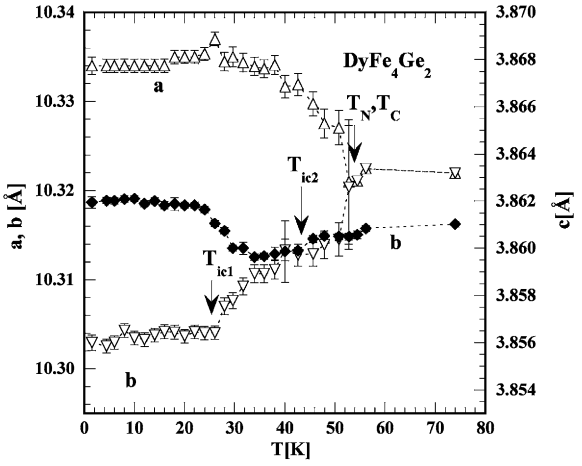

Fig. 4. Thermal variation of the lattice parameters as derived from neutron data referred to the orthorhombic *Cmmm* ($a_t\sqrt{2}$, $a_t\sqrt{2}$, c_t) cell. Anomalies are visible at the three transition temperatures $T_{N,c}$, T_{ic1}, T_{ic2}. The lines are guides to the eyes.

However, scaling the parameters by the scale factor $a_{XR}/a_{neutron}$ at 15 K results to a mismatch of the b and c parameters in the IT range T_{ic1}–T_{ic2} between the two independent measurements while the behaviour of the a lattice constant is reproducible by the two methods. This fact can be explained only by the presence of hysteresis phenomena for the b and c parameters, in the IT temperature interval, related to the re-entrant isostructural first order transition on heating from the LT lock-in magnetic phase ($\mathbf{q}_1 = (0\,\frac{1}{2}\,0)$) at $T_{ic1} = 28$ K to the incommensurately modulated phase ($\mathbf{q}_2 = (0 q_y 0)$); which, in turn, transforms back to the HT lock-in structure above $T_{ic2} = 45$ K. The latter transition affects slightly the a-axis as derived in Part I. Similar hysteresis phenomena related to first order isostructural transitions have been reported also for other systems [11].

The first-order nature of the LT lock-in transition can be confirmed by the coexistence of two magnetic wave vectors at $T_{ic1} = 28$ K as well as at 46 K, which is just above the transition temperature $T_{ic2} = 45$ K; see Figs. 1 and 2a, b (middle part).

3.5. Thermal variation of the refined magnetic parameters

3.5.1. The wave vector

The indexing of the magnetic reflections as well as their positional changes over the entirely ordered regime can now be fully described by the thermal variation of the wave vector length and of the lattice parameters (see Figs. 4 and 5). The latter figure shows clearly that the magnetically ordered state comprises three ranges of distinct magnetic order, namely the LT interval: 1.5 K $- T_{ic1} =$ 28 K; the IT interval: $T_{ic1} - T_{ic2} = 45$ K and the HT interval: $T_{ic2} - T_{N,c}$. The LT and HT magnetic phases have the same commensurate wave vector $\mathbf{q}_1 = (0\,\frac{1}{2}\,0)$ while the wave vector of the IT phase is incommensurate with the crystal lattice $\mathbf{q}2 = (0\,q_y\,0)$. Fig. 5 shows, that in the IT range the wave vector length displays a re-entrant behaviour with temperature. In more detail at $T_{ic1} = 28$ K $\mathbf{q}_1$ jumps on heating from $(0\,\frac{1}{2}\,0) \rightarrow$ to $\mathbf{q}_2 = (0\,0.440\,0)$ and then continues to decrease more slowly down

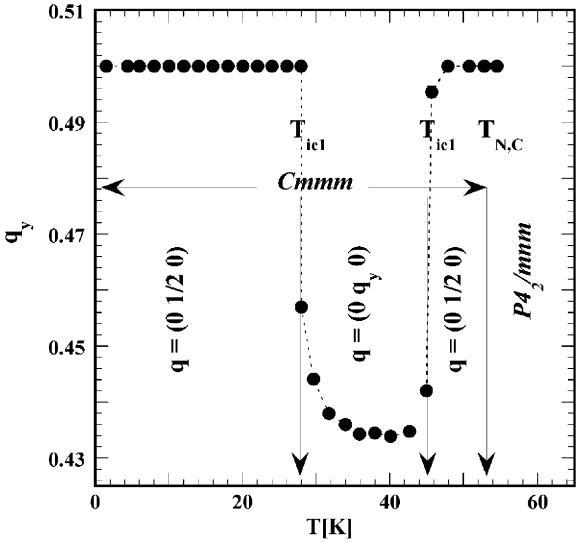

Fig. 5. Temperature dependence of the $\mathbf{q}_2 = (0\,q_y\,0)$ wave vector length sandwiched between two lock-in phases $\mathbf{q}_1 = (0\,\frac{1}{2}\,0)$ the HT $T_N > T > T_{ic2}$ and LT $T < T_{ic1} = 28$ K magnetic phases. The dotted line is a guide for the eye.

to 36 K to (0 0.4339 0). It remains almost unchanged in the range 36–40 K. Above 40 K the wave vector length increases again slowly till $T_{ic2} = 45$ K where it jumps back to the commensurate value $(0\,\frac{1}{2}\,0)$. The sequence of phases is summarised in the magnetic phase diagram of Fig. 8.

3.5.2. The thermal variation of magnetic structural parameters

The thermal behaviour of the model dependent magnetic parameters is displayed in Fig. 6. Our results have to be seen within the frame of the imposed parameter constraints, as described in the previous sections, in view of the feasibility of the refinements. Some of these constraints may be removed when data with higher flux and instrumental resolution become available. The thermal evolution of the ordered moment amplitude (Fourier coefficients) shows that the Dy and Fe sites order simultaneously. The Fe moments reach saturation already at 36 K while the Dy moments reach saturation only below 20 K. In the HT range T_{ic2}–T_N the moments of the Dy and Fe sites were

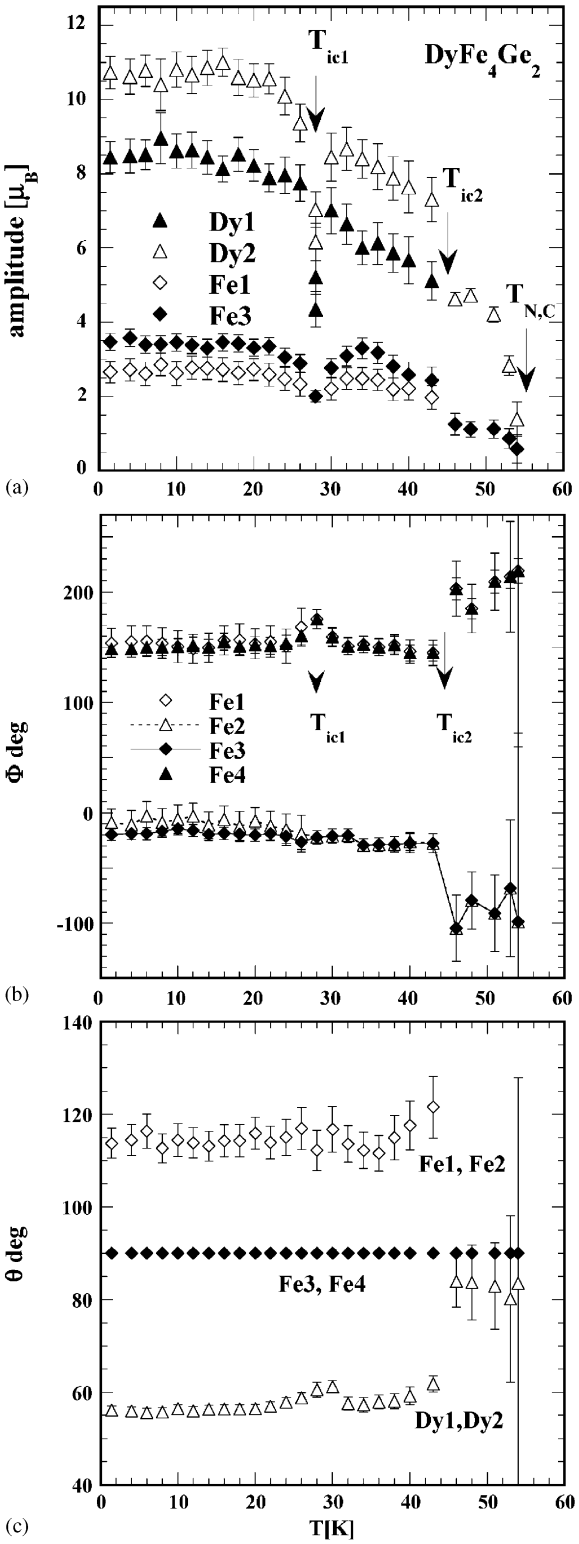

Fig. 6. Refined parameters relevant to magnetic order as a function of temperature. The amplitude of the Fourier coefficients of the Dy and Fe sites (a), the Fe moment angles Φ with the a axis (b) and the angle θ of the Dy and the Fe moments with the c axis (c). at $T_{ic1} = 28$ K and $T_{ic2} = 45$ K (on cooling). The lines are guides to the eye.

constraint to the same value and the angle θ with the c-axis to 90° which corresponds to a collinear Dy moment arrangement along b and to a planar canted arrangement for Fe. The HT isostructural magnetic transition at $T_{ic2} = 45$ K is characterised by a spin reorientation of both the Dy and Fe sublattices. Just below T_{ic2} the wave vector becomes incommensurate with the crystal lattice and the moments of the Dy1 and Dy2 sites rotate within the (1 0 0) plane away from the b-axis. Thus the moment angle θ to the c-axis jumps from 90° → 60° towards the c-axis. Below T_{ic2} the θ angle changes only slightly to 57° down to 1.5 K with minor fluctuations around $T_{ic1} = 28$ K. The $Fe3_i$ and $Fe4_i$ orbits display a planar arrangement ($\theta = 90°$) over the entire magnetically ordered regime while the θ angle of the $Fe1_i$ and $Fe2_i$ orbits changes in opposite direction to that of Dy from 90° $T_{ic2} \rightarrow 125°$ at 40 K → 112° at 36 K and remaining within error unchanged down to 1.5 K. A further spin reorientation is seen within the (0 0 1) plane Fig. 6(c). The angle Φ of $Fe1_i$ and $Fe4_i$ from 155° in the LT range 1.5 K − $T_{ic2} \rightarrow 185°$ in the IT range $T_{ic2} - T_N$ and that of $Fe2_i$ and $Fe3_i$ from −20° in the LT range $1.5 - T_{ic2} \rightarrow -100°$ in the IT range $T_{ic2} - T_N$. These changes indicate that in the coplanar HT lock-in phase the Fe moments, within a Fe tetrahedron, have a ferrimagnetic arrangement while in the LT lock-in this arrangement is more close to antiferromagnetic.

4. Discussion

The magnetic phase diagram displayed in Fig. 8 summarises the results of the present investigation and partly those of Part (I). The compound $DyFe_4Ge_2$ was found to undergo a simultaneous second order magnetostructural transition at

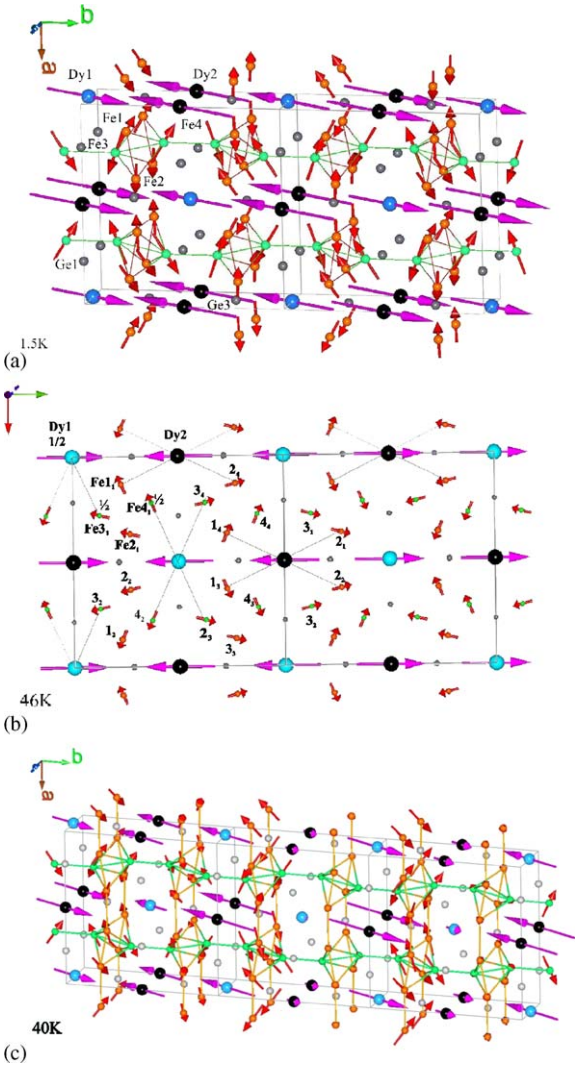

Fig. 7. Schematic representation of (a) The lock-in (LT) phase, $\mathbf{q}_1 = (0\,\frac{1}{2}\,0)$, at 1.5 K. (b) The lock-in (HT) orthorhombic, $\mathbf{q}_1 = (0\,\frac{1}{2}\,0)$, phase at 46 K. (c) The incommensurate (IT) magnetic structure at 31 K, $\mathbf{q}_2 = (0\,q_y\,0)$ of $DyFe_4Ge_2$.

$T_N, T_c = 55$ K followed by two first order isostructural magnetic transitions at lower temperatures $T_{ic2} = 45$ K and $T_{ic1} = 28$ K:

$$Cmmm(LT),\ \mathbf{q}_1 = (0\,\tfrac{1}{2}\,0) T_{ic1} = 28\,\mathrm{K} \Rightarrow (IT),$$
$$\mathbf{q}_2 = (0\,q_y\,0) T_{ic2} = 45\,\mathrm{K} \Rightarrow (HT) : \mathbf{q}_1 = (0\,\tfrac{1}{2}\,0).$$

4.1. Comparison of neutron diffraction results with mössbauer and magnetic measurements

Our results show that the Fe and Dy moments order simultaneously but reach saturation the former at 36 the latter at 20 K. Our results differ to those of the magnetic measurements and Mössbauer effect on the long range ordering temperature 55 K which is lower to the value $T_N =$ 65K derived by fitting Mössbauer data with a Brillouin function [2]. Furthermore the refined 4.2 K ordered moment values of Dy are reduced (6 μ_B/atom for Dy1 and 7.5 μ_B/atom for Dy2), and much larger for Fe (1.8 and 2.4 μ_B/atom for the $Fe1_i$, $Fe2_i$ sites and the $Fe3_i$, $Fe4_i$ sites respectively) if compared to the average values 10.17 μ_B/Dy given in [3] and 0.53 μ_B/Fe atom [2]. As explained in [3] these differences might be related to the transferred hyperfine field of the Fe sublattice. The Dy moments are reduced if compared to the Dy^{3+} free ion value $gJ\,\mu_B = 10\,\mu_B$ presumably due to crystal field effects. Furthermore the present results do not confirm the c-axis anisotropy reported for Dy in [3] it seems rather that the anisotropy is along the b-axis instead. The moments of both Dy sites have the same angle θ with the c axis over the entire magnetically ordered regime which is 90° for T_{ic2}–T_N and about 60° below $T_{ic2} = 45$ K. The Fe moment values compare favourably to the values obtained for the Ho and Er isomorphic compounds but are much larger than the value found in the Y compound. This indicates that the Fe ordering is enhanced by the R-Fe magnetic interaction.

The saturation average moment value found in [2] of 8 μ_B/f.u. in a field of 40 T at 4.2 K compared to our results (Table 4) indicates that at this field the system remains ferrimagnetic. A ferromagnetic arrangement for the Fe moments would correspond to 8.5 and to 6.8 μ_B/f.u for Dy which makes 15.3 μ_B/f.u in total. This means that if all Fe and all Dy sublattices became ferromagnetic the angle among them would be 118° and the Fe–Dy antiferromagnetic interaction prevails at low temperatures. However, in view of the similar value of the ordering temperatures of the isomorph RFe_4Ge_2 compounds the Fe–Fe antiferromagnetic interactions might be important in the HT range.

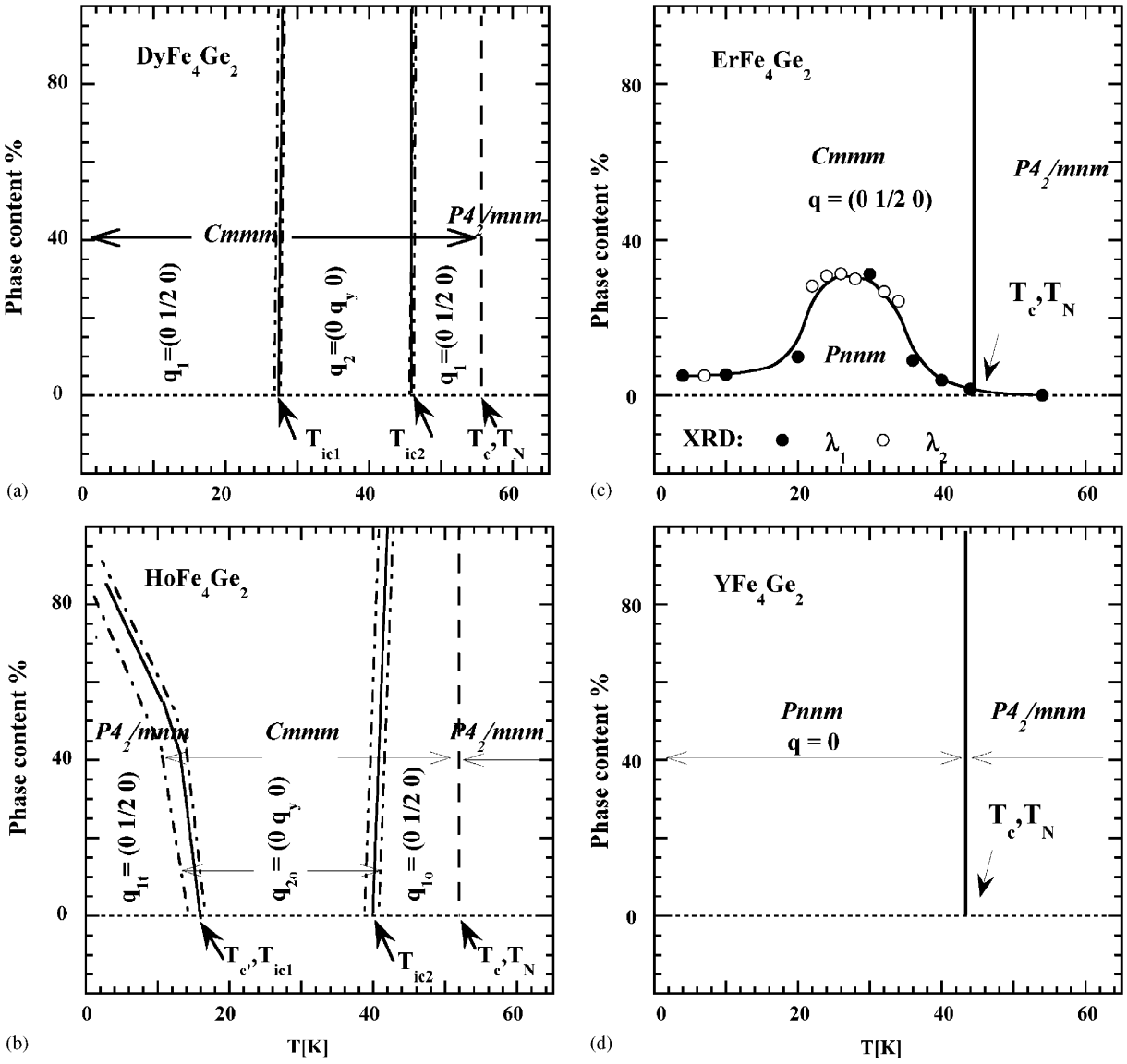

Fig. 8. Schematic representation of the structural and magnetic phase diagram of $DyFe_4Ge_2$ (a) The magnetic phase diagrams of $HoFe_4Ge_2$ (b) $ErFe_4Ge_2$ (c) and YFe_4Ge_2 (d) are also shown. Full and dashed lines indicate first- and second order transitions. Dash dotted lines denote the lower and upper limit of coexistence regions around the first order transitions ($T_{c'}$,T_{ic1}, and T_{ic2}) of the adjacent magnetic and/or crystal structures.

4.2. Comparison of RFe_4Ge_2 ($R = Y$, Er, Ho, Dy) phase diagrams

4.2.1. HT range

The phase diagrams of the compounds investigated up to now (Fig. 8) show that the *HT* double transition (magnetostructural) $P4_2/mnm\, T_N, T_c \rightarrow Cmmm(\mathbf{q} = (0\tfrac{1}{2}0))$ is typical for the magnetic rare earth isomorphic compounds as it occurs for $HoFe_4Ge_2$, and $DyFe_4Ge_2$ as well as partly on $ErFe_4Ge_2$ but not in the nonmagnetic Y. The occurrence of the wave vector $(0\tfrac{1}{2}0)$ is the result of

a complex system of exchange interactions, whereas all R–R interactions are positive (ferro) within the planes perpendicular *ac* plane, along *b*, the nearest neighbour Dy1-Dy2 (see Fig. 7b) interactions, change sign in an alternate sequence ($+\ +\ -\ -+\ +\ -\ -+\ +\ -\ -\ \ldots$) but the second neighbour interaction Dy1–Dy1 along *b* is antiferromagnetic, which leads to 2*b* doubling. This implies a more complex set of exchange interactions involving the whole set of magnetic atoms. Here it should be noted that the spontaneous shear strain $e_2 = e_{xy}$ resulting from the ferroelastic transition is most likely related to the R in-plane components which are constraint to the tetragonal mirror plane m_{xxz} or to the orthorhombic m_x and most likely induce the transition. These planes are exclusively occupied by R and Ge atoms. However the LT range is different for all of them.

4.2.2. IT and LT ranges

The $ErFe_4Ge_2$ magnetic phase diagram of the *Cmmm* phase has a single commensurate wave vector $\mathbf{q}_1 = (0\,\frac{1}{2}\,0)$ down to 1.5 K. A spin reorientation transition has been found below $T_{ic1} = 8$ K. For $T > T_{ic1}$ the Er moments are close to the *c*-axis and a spin reorientation below 8 K moves the moment away from the *c*-axis. For this compound the behaviour of the IT as well as HT ranges for $T > 26$ K will be revised in a future communication by implementing the coexistent second structure *Pnnm* found by high-resolution X-ray data in the mean time [5]. The compounds $HoFe_4Ge_2$ and $DyFe_4Ge_2$ display three distinct regions of magnetic ordering, that are also connected with spin reorientations. The $DyFe_4Ge_2$ phase diagram has two *Cmmm* lock–in phases with the same vector $\mathbf{q}_1 = (0\,\frac{1}{2}\,0)$ a HT and a LT and an incommensurate IT phase $\mathbf{q}_2 = (0\,q_y\,0)$. The *Cmmm* phase for $HoFe_4Ge_2$ has only a HT lock-in phase $\mathbf{q}_{1o} = (0\,\frac{1}{2}\,0)$ and an incommensurate phase below $T_{ic2} = 40K$ with $\mathbf{q}_2 = (0\,q_y\,0)$. The LT lock-in phase occurring at $T_{ic1} = 15$ K and $\mathbf{q}_{1t} = (0\,\frac{1}{2}\,0)$ refers to the re-entrant tetragonal (LT) phase. Here, it should be noted that in both the Ho and Dy compounds below the LT lock-in transition in the *Cmmm* phase the *c*-axis has a negative expansion. On the other hand for $HoFe_4Ge_2$ the *Cmmm* phase exists only as a metastable phase below T_{ic1}. Within the range T_{ic2} down to 1.5 K the wave vector of $HoFe_4Ge_2$ decreases linearly while for $DyFe_4Ge_2$ it displays a re-entrant behaviour in the range $T_{ic1} - T_{ic2}$ so that below T_{ic1} it jumps to the commensurate value $\frac{1}{2}$. Apparently the occurrence of a re-entrant magnetic phase is intimately connected to the unusual thermal evolution of the incommensurate wave vector length.

4.3. Comparing the Dy magnetic structures

The $DyFe_4Ge_2$ HT 2D canted lock-in magnetic phase undergoes on cooling at $T_{ic2} = 45$ K a first-order isostructural magnetic transition to an incommensurate IT magnetic phase stable in the temperature range $T_{ic2} - T_{ic1} = 28$ K. This transition is related to a jump of the q_y wave vector component from $\frac{1}{2}$ to an incommensurate value $q_y \approx 0.44$, and a spin reorientation of the Dy moments away from the *b*-axis and towards the *c*-axis. The spin reorientation might be related to high-order terms of the crystal field induced Dy sublattice anisotropy that become important at lower temperatures as in the compound with Er. Simultaneously the HT planar ferrimagnetic arrangement of the Fe moments within the compact tetrahedra becomes progressively more close to antiferromagnetic on further cooling below $T_{ic2} = 45$ K due to in-plane rotation of the Fe moments till about 36 K where the Fe moments reach saturation and $q_y \approx 0.433$. Below 36 K the wave vector starts again to increase anew and jumps back at 28 K to the HT value $q_y = \frac{1}{2}$. The refined X-ray cell parameters showed a haphazard behaviour of the tetrahedron torsion angle and of the out of plane Fe–Fe distances in the magnetically ordered regime that accompany the magnetic transitions. Incommensurately modulated phases are a common phenomenon in rare earth alloys [12] and occur as a consequence of the competition between the oscillatory character of the indirect RKKY exchange interaction mediated via the polarisation of the conduction band electrons, which is responsible for the long-range magnetic ordering and the crystalline field anisotropy. For rare-earth atoms with an odd numbers of unpaired electrons, as for Dy and Er (Kramer's ions),

amplitude-modulated structures may become unstable at $T = 0\,K$ and the wave vector jumps to the lock-in value or the structure squares-up. However, for non Kramer's ions as for Ho the incommensurate amplitude modulated phase may be stable down to 0 K when the lowest crystal-field state is a nonmagnetic singlet [12]. In the presently investigated materials, the sequence of phases is a non-standard one, the incommensurate range being below the *HT* commensurate phase in $HoFe_4Ge_2$ and also in $DyFe_4Ge_2$ it is sandwiched between a commensurate *HT* phase and the *LT* lock-in phase.

The *LT* 3D magnetic structure is characterised by almost antiferromagnetic Fe–Fe nearest neighbour interactions in the Fe compact tetrahedra and antiferromagnetic Dy–Fe arrangement. The Fe moments try to orient themselves anti-parallel or perpendicular to the adjacent rare earth moment located on the centre of an oblong square with Fe atoms at his corners (see Fig. 7b). This arrangement creates a weak molecular field at the rare earth position.

A complete study of the relative strength of the exchange interactions and anisotropy terms is out of the scope of the present paper, but it is clear that such a study is worth to be undertaken for understanding the complex magnetic behaviour observed in this family of compounds.

References

[1] P. Schobinger-Papamantellos, J. Rodríguez-Carvajal, G. André, N.P. Duong, K.H.J. Buschow, P. Tolédano, J. Magn. Magn. Mater. 236 (2001) 14.
[2] A.M. Mulders, P.C.M. Gubbens, Q.A. Li, F.R. de Boer, K.H.J. Buschow, J. Alloys Compounds. 221 (1995) 197.
[3] .P.C.M. Gubbens, B.D. van Dijk, A.M. Mulders, S.J. Harker, K.H.J. Buschow, J. Alloys Compounds. 319 (2001) 1.
[4] P. Schobinger-Papamantellos, J. Rodríguez-Carvajal, G. André, C.H. de Groot F.R. de Boer, K.H.J. Buschow, J. Magn. Magn. Mater. 191 (1999) 261.
[5] P. Schobinger-Papamantellos, J. Rodríguez-Carvajal, K.H.J. Buschow, E. Dooryhee, A.N. Fitch, J. Magn. Magn. Mater. 210 (2000) 121.
[6] P. Schobinger-Papamantellos, J. Rodríguez-Carvajal, K.H.J. Buschow, E. Dooryhee, A.N. Fitch, J. Magn. Magn. Mater. 250 (2002) 225.
[7] P. Schobinger-Papamantellos, J. Rodríguez-Carvajal, G. André, C. Ritter, K.H.J. Buschow, J. Magn. Magn. Mater. 280 (2004) 119.
[8] J. Rodríguez-Carvajal, Physica B 192 (1993) 55 The programs of the *FullProf Suite* and their corresponding documentation can be obtained from the Web at ftp://ftp.cea.fr/pub/llb/divers/fullprof.2k/.
[9] L.C. Chapon, J. Rodríguez-Carvajal (unpublished). *FullProf Studio* is a program of the *FullProf Suite* that is freely available in the site given in Ref [8].
[10] J. Rossat-Mignod, in: Methods of Experimental Physics: Neutron Scattering, Vol. 3, Academic Press, New York, 1987.
[11] A.R. Oganov, G.D. Price, J.P. Brodholt, Acta Crystallogr. A 57 (2001) 548.
[12] D. Gignoux, D. Schmitt, Phys. Rev. B 48 (17) (1993) 12682.